

Reproducing the stellar-mass dependence of the giant planet occurrence rate with pebble accretion models

Heather F. Johnston,^{1,2*} O. Panić,² S. Reffert,³ B. Liu⁴ and X. Ma,¹

¹ *Department of Physics and Astronomy, University of Exeter, Stocker Road, Exeter EX4 4QL, UK*

² *School of Physics and Astronomy, University of Leeds, Woodhouse, Leeds LS2 9JT, England*

³ *Landessternwarte, Zentrum für Astronomie der Universität Heidelberg, Königstuhl 12, 69117 Heidelberg, Germany*

⁴ *Astronomical Institute, School of Physics, Zhejiang University, 38 Zheda Road, Hangzhou, 310027 China*

Accepted XXX. Received YYY; in original form ZZZ

ABSTRACT

The stellar mass dependence of the unbiased giant planet occurrence rate may be the best statistical tool to constrain the formation of such planets. This rate rises and falls as a function of stellar mass, peaking around stars of $\sim 1.7\text{--}2 M_{\odot}$. In this work, we carry out a population synthesis study, using pebble-driven core accretion model of planet formation, to investigate the planet formation conditions that may be responsible for this stellar-mass dependence. We use the inferred giant planet occurrence rate of three combined homogenised radial velocity surveys (EXPRESS, PPPS, and Lick giant star survey) to constrain the models. We find that we can produce a synthetic giant planet population with closely aligned occurrence and properties when we base our model on observationally-supported assumptions that accretion rates are higher and disk lifetimes are shorter around more massive stars, we can produce a synthetic giant planet population with closely aligned properties to the observed distribution. We also find that in this scenario, the runaway gas accretion occurs at a larger orbital distance and earlier times as the stellar mass increases.

Key words: planets and satellites: formation – stars: planetary systems – methods: numerical

1 INTRODUCTION

Giant planets - while being only observed around 10–20% of stars (Cumming et al. 2008; Johnson et al. 2010; Mayor et al. 2011) - play a vital role in shaping the architecture of planetary systems that host them. Studying the conditions of their formation is pivotal in furthering our understanding of dynamics and habitability of planetary systems, including our own Solar System (Liu et al. 2022b).

The occurrence rate of giant planets η_J is found to increase with stellar metallicity across both main-sequence and evolved stars (Gonzalez 1997; Santos et al. 2001, 2004; Fischer & Valenti 2005; Udry & Santos 2007; Johnson et al. 2010; Sousa et al. 2011; Mortier et al. 2012, 2013; Reffert et al. 2015; Wolthoff et al. 2022; Pan et al. 2025). Ghezzi et al. (2018) propose that the probability of giant planet formation is around one-to-one for the total amount of metals in the protoplanetary disk. Their sample of evolved A-stars, along with FGKM dwarfs, confirms that η_J increases with both metallicity and stellar mass up to $2 M_{\odot}$ (Ghezzi et al. 2018).

However, while radial velocity (RV) surveys have surmised that η_J increases with stellar mass between $0.5\text{--}2 M_{\odot}$ (Johnson et al. 2010; Bowler et al. 2010; Borgniet et al. 2019) - this does not hold for stars more massive than $2 M_{\odot}$. Reffert et al. (2015) and Jones et al. (2015) both reported a likely peak in η_J at $1.5\text{--}2 M_{\odot}$ that drops quickly for more massive stars. Giant planets are incredibly rare around stars more massive than $2.5 M_{\odot}$ ($\eta_J \sim 0$). Additionally, in Wolthoff et al. (2022), they combined data from three different

RV surveys (EXPRESS, PPPS, and Lick giant star survey) placed the peak of η_J around stars of $1.7 M_{\odot}$. Direct imaging surveys have also inferred that the frequency of giant planets increases with stellar mass (Wagner et al. 2022).

The exact origin of the stellar mass dependence of η_J rate is still unclear. Kennedy & Kenyon (2009) were among the first to discuss possible physical reasons for the paucity of giant planets around massive stars, noting that faster disk dispersal, lower disk surface densities at large orbital radii, and slower orbital speeds all act to suppress giant planet formation at higher stellar masses. The lifetimes of protoplanetary disks, driven by pre-main sequence (PMS) stellar evolution, are thought to have major influence over the success of giant planet formation - and resulting η_J rate. Giant planets require gas to form, and sufficient gas is only available during the protoplanetary disk stage. The luminosity evolutionary tracks of PMS stars with $M_{\star} \geq 1.5 M_{\odot}$ differ significantly from their solar-mass counterparts, even at young ages. Low-mass stars decrease in luminosity as they evolve towards the main sequence. In contrast, stars with masses $\geq 1.5 M_{\odot}$ increase in luminosity as they approach the main sequence, warming their disks within a few Myr (Miley et al. 2020). This elevated disk temperature increases the gas scale height, reducing pebble accretion efficiency and slowing planet formation (Johnston et al. 2025).

In this paper, we use the pebble-driven core accretion planet formation model from Liu et al. (2019) and Johnston et al. (2024) to reproduce the observed planet occurrence rates as a function of mass and metallicity, derived in the studies by Reffert et al. (2015); Wolthoff et al. (2022), through planet population synthesis. For each

* E-mail: h.johnston2@exeter.ac.uk (UoE)

stellar mass-metallicity combination in the RV observed sample of [Wolthoff et al. \(2022\)](#), we conduct 100 numerical simulations of the growth of single embryos.

The aim of this work is to reproduce the giant planet occurrence rate from the observations via planet population synthesis using our model and establish the reasons behind the distribution of the giant planet population ([Reffert et al. 2015](#); [Wolthoff et al. 2022](#)). In order to do this, we seek to identify the key physical properties that drive the rise and fall of the giant planet occurrence rate as a function of stellar mass. The paper is organised as follows. The key principles of the model are described in Section 2. In Section 3, we recount the setup of the model and our relevant assumptions. Section 4 discusses the results of our population synthesis study and compare to the giant planet occurrence rate as functions of stellar mass and metallicity. Penultimately, we discuss where and when our giant planets accrete the bulk of their mass and how the orbital distances of our synthetic giant planet population compare to the observed distances in Section 5. In Section 6, our final conclusions are drawn and summarised.

2 METHOD

We employ the planet formation model of [Liu et al. \(2019\)](#), originally adapted in [Johnston et al. \(2024\)](#), and summarise the key equations in this section. Readers are recommended to go through their Section 2 for details. The disk condition presented here are adapted to host stars of masses 0.9–5 M_\odot , with the addition of evolving stellar luminosity, in order to encompass the stellar mass range from the observed RV sample in [Wolthoff et al. \(2022\)](#).

2.1 Disk model

We adopt a conventional α viscosity prescription for the gas disk angular momentum transport ([Shakura & Sunyava 1973](#)). The disk accretion and surface density are linked through $\dot{M}_g = 3\pi r \Sigma_g$ with viscosity $\nu = \alpha_g c_s H_g$, where $c_s = H_g \Omega_K$ is the sound speed, H_g is the gas disk scale height and Ω_K is the Keplerian frequency. The dimensionless viscous coefficient α_g determines the global disk evolution and gas surface density. We set it to be a fixed value of 10^{-2} , the same as [Liu et al. \(2019\)](#); [Johnston et al. \(2024\)](#).

The evolution of the disk accretion rate is expressed as

$$\dot{M}_g = \begin{cases} \dot{M}_{g0} \left[1 + \frac{t}{\tau_{\text{vis}}} \right]^{-\gamma}, & t < t_{\text{pho}}, \\ \dot{M}_{g0} \left[1 + \frac{t}{\tau_{\text{vis}}} \right]^{-\gamma} \exp \left[-\frac{t - t_{\text{pho}}}{\tau_{\text{pho}}} \right], & t \geq t_{\text{pho}}, \end{cases} \quad (1)$$

where \dot{M}_{g0} is the initial disk accretion rate; the $t - t_{\text{pho}}$ term refers to the mass loss due to stellar photoevaporation; τ_{vis} and τ_{pho} are the characteristic viscous accretion and photoevaporation timescales from Eqs. (3) and (7) of [Liu et al. \(2019\)](#), $\gamma = (5/2 + s)/(2 + s)$, and s is the gas surface density gradient.

We specifically account for the X-ray driven photoevaporation, and the critical mass-loss rate is given by ([Owen & Jackson 2012](#))

$$\frac{\dot{M}_{\text{pho}}}{M_\odot \text{yr}^{-1}} = 6 \times 10^{-9} \left(\frac{M_\star}{1 M_\odot} \right)^{-0.07} \left(\frac{L_X}{30 \text{ ergs}^{-1}} \right)^{1.14} \\ = 3 \times 10^{-8} \left(\frac{M_\star}{2.4 M_\odot} \right)^{1.6}, \quad (2)$$

where we have substituted the $L_X - M_\star$ relation from [Owen & Jackson \(2012\)](#) to obtain the second line.

We employ a two-component disk structure, including an inner

viscously heated region and an outer stellar irradiated region. The gas surface density and disk aspect ratio are adopted from Eqs. (8)-(13) of [Liu et al. \(2019\)](#), where [vis] refers to the inner viscously heated disk and [irr] refers to the outer disk region heated entirely by stellar irradiation (where the disk is optically thin):

$$\frac{\Sigma_g}{\text{g cm}^{-2}} = \begin{cases} 480 \left(\frac{\dot{M}_g}{10^{-7} M_\odot \text{yr}^{-1}} \right)^{1/2} \left(\frac{M_\star}{2.4 M_\odot} \right)^{1/8} \\ \left(\frac{r}{1 \text{ au}} \right)^{-3/8} & \text{[vis]}, \\ 1440 \left(\frac{\dot{M}_g}{10^{-7} M_\odot \text{yr}^{-1}} \right) \left(\frac{M_\star}{2.4 M_\odot} \right)^{9/14} \\ \left(\frac{L_\star}{2.4^4 L_\odot} \right)^{-2/7} \left(\frac{r}{1 \text{ au}} \right)^{-15/14} & \text{[irr]}, \end{cases} \quad (3)$$

$$h_g = \begin{cases} 0.043 \left(\frac{\dot{M}_g}{10^{-7} M_\odot \text{yr}^{-1}} \right)^{1/4} \left(\frac{M_\star}{2.4 M_\odot} \right)^{-5/16} \\ \left(\frac{r}{1 \text{ au}} \right)^{-1/16} & \text{[vis]}, \\ 0.025 \left(\frac{M_\star}{2.4 M_\odot} \right)^{-4/7} \left(\frac{L_\star}{2.4^4 L_\odot} \right)^{1/7} \\ \left(\frac{r}{1 \text{ au}} \right)^{2/7} & \text{[irr]}. \end{cases} \quad (4)$$

The temperature profile of the disk follows:

$$\frac{T_g}{\text{K}} = \begin{cases} 280 \left(\frac{\dot{M}_g}{10^{-7} M_\odot \text{yr}^{-1}} \right)^{1/2} \left(\frac{M_\star}{2.4 M_\odot} \right)^{3/8} \\ \left(\frac{\alpha_g}{10^{-2}} \right)^{-1/4} \left(\frac{\kappa_0}{10^{-2}} \right)^{-1/4} \left(\frac{r}{1 \text{ au}} \right)^{-9/8} & \text{[vis]}, \\ 236 \left(\frac{M_\star}{2.4 M_\odot} \right)^{-1/7} \left(\frac{L_\star}{2.4 L_\odot} \right)^{2/7} \\ \left(\frac{r}{1 \text{ au}} \right)^{-1/2} \phi_{\text{inc}}^{1/4} & \text{[irr]}, \end{cases} \quad (5)$$

where M_\star , L_\star are stellar mass and luminosity, and r is the radial distance to the central star. The transition radius between these two disk regions is written as

$$r_{\text{tran}} = 4.9 \left(\frac{\dot{M}_g}{10^{-7} M_\odot \text{yr}^{-1}} \right)^{28/39} \left(\frac{M_\star}{2.4 M_\odot} \right)^{29/39} \\ \left(\frac{L_\star}{2.4^4 L_\odot} \right)^{-16/39} \text{ au}. \quad (6)$$

The main disk solid reservoir - pebbles - are assumed to be constituted of 35% water ice and 65% silicate ([Liu et al. 2019](#)). The water-ice line $r_{\text{H}_2\text{O}}$ is derived by equating the saturated pressure and H_2O vapor pressure (approximately in the disk radius at the temperature of 170 K).

We do not account for any detailed grain growth processes. Instead, we assume that the dust has already fully grown and treat their final size to be a free parameter, indicative as either a fixed physical size or a fixed Stokes number. The above simplification ideally mimics the grain growth is limited by the bouncing or fragmentation barriers ([Güttler et al. 2010](#)).

The inner edge of the disk is truncated by the stellar magnetospheric torque ([Lin et al. 1996](#)). We approximate the co-rotation cavity radius of the host star from [Mulders et al. \(2015\)](#) as:

$$r_{\text{in}} = \sqrt[3]{\frac{GM_{\star}}{\Omega_{\star}^2}} \simeq 0.06 \left(\frac{M_{\star}}{2.4 M_{\odot}} \right)^{1/3} \text{ au}, \quad (7)$$

where Ω_{\star} is the stellar spin frequency.

In our model, the inner disk edge acts as the point at which inward migration and solid accretion are halted. This cutoff location from Mulders et al. (2015) is in the range of ~ 0.05 – 0.1 au, depending on stellar mass, and is in agreement with the recent models from Flock et al. (2019) for FGK and M-type stars.

2.2 Planet growth and migration

Core mass growth proceeds via pebble accretion. Embryo formation is treated through streaming instability, a powerful mechanism that forms planetesimals from the collapse of many mm-sized pebbles (Youdin & Goodman 2005). It is a method that is particularly effective at forming planetesimals (Johansen et al. 2007, 2012; Bai & Stone 2010; Simon et al. 2016; Schäfer et al. 2017; Abod et al. 2019; Li et al. 2019). Liu et al. (2020) summarised from the literature that streaming instability planetesimal formation simulations show the birth masses of embryos depend on their evolutionary time and disk locations, which can be expressed as:

$$\frac{M_{\text{p}0}}{M_{\oplus}} = 6 \times 10^{-2} (\gamma\tau)^{1.5} \left(\frac{h_{\text{g}}}{0.05} \right)^3 \left(\frac{M_{\star}}{2.4 M_{\odot}} \right). \quad (8)$$

The self-gravity parameter γ that quantifies the relative strength between the gravity and tidal shear is given by

$$\gamma \equiv \frac{4\pi G \rho_{\text{g}}}{\Omega_{\text{K}}^2}. \quad (9)$$

The solid accretion rate onto the planet's core reads

$$\dot{M}_{\text{PA}} = \epsilon_{\text{PA}} \dot{M}_{\text{peb}} = \epsilon_{\text{PA}} \xi \dot{M}_{\text{g}}, \quad (10)$$

where ϵ_{PA} is the efficiency of pebble accretion, the formulas of which are adopted from Liu & Ormel (2018) and Ormel & Liu (2018) that include both 2D and 3D regimes and expressed as:

$$\epsilon_{\text{PA}} = \sqrt{\epsilon_{\text{PA},2\text{D}}^2 + \epsilon_{\text{PA},3\text{D}}^2}, \quad (11)$$

where $\epsilon_{\text{PA},2\text{D}}$ and $\epsilon_{\text{PA},3\text{D}}$ are defined from Liu & Ormel (2018) and Ormel & Liu (2018), respectively.

The pebble scale height is given by:

$$H_{\text{peb}} = \sqrt{\frac{\alpha_{\text{t}}}{\alpha_{\text{t}} + \tau_{\text{s}}}} H_{\text{g}}, \quad (12)$$

where τ_{s} is the Stokes number of the particles and α_{t} is the turbulent diffusion coefficient, approximately equivalent to the midplane turbulent viscosity when the disk is driven by magnetorotational instability (Johansen & Klahr 2005; Zhu et al. 2015; Yang et al. 2017).

Whether pebble accretion is in 2D or 3D depends on the ratio between the radius of pebble accretion and the vertical layer of pebbles (Morbidelli et al. 2015).

Similar to Liu et al. (2019, 2020), we assume that the pebble and gas flux ratio remains a constant such that $\xi = \dot{M}_{\text{peb}}/\dot{M}_{\text{g}}$. When pebbles have a low Stokes number, they are well-coupled to the disk gas and drift inwards at the same rate, such that the pebble-to-gas surface density ratio reflects the initial disk metallicity. When the Stokes number is high, pebbles drift faster than the gas, and in order to maintain a constant flux ratio, $\Sigma_{\text{peb}}/\Sigma_{\text{g}}$ falls below the nominal disk

metallicity. We neglect the metallicity enrichment in the late rapid gas removal phase when the stellar photoevaporation dominates.

A growing planet begins to clear the surrounding gas and open a partial gaseous annular gap, causing the inward pebble flux to be halted at the outer edge of the planetary gap and solid accretion to terminate (Lambrechts et al. 2014). This planetary mass threshold is referred to as the pebble isolation mass, and we adopt the formula from Bitsch et al. (2018):

$$M_{\text{iso}} = 16 \left(\frac{h_{\text{g}}}{0.03} \right)^3 \left(\frac{M_{\star}}{3 M_{\odot}} \right) \left[0.34 \left(\frac{-3}{\log_{10} \alpha_{\text{t}}} \right)^4 + 0.66 \right] \left[1 - \frac{\partial \ln P / \partial \ln r + 2.5}{6} \right] M_{\oplus}. \quad (13)$$

We note that a non-negligible fraction of pebble fragments at the above-mentioned planetary gap can still pass through and replenish the planetary envelope (Chen et al. 2020) as well as the inner disk region (Liu et al. 2022a; Markus Stammerl et al. 2023). We do not model this effect here.

When the low-mass planets still accrete pebbles, the solid materials entering the planetary atmosphere would generate sufficient heating to prevent the further contraction of the surrounding gas. Therefore, we only follow the gas accretion when the planet grows beyond M_{iso} . The gas accretion rate can be expressed as

$$\dot{M}_{\text{p,g}} = \min \left[\left(\frac{dM_{\text{p,g}}}{dt} \right)_{\text{KH}}, \left(\frac{dM_{\text{p,g}}}{dt} \right)_{\text{Hill}}, \dot{M}_{\text{g}} \right]. \quad (14)$$

We adopt the gas accretion rate based on Ikoma et al. (2000):

$$\left(\frac{dM_{\text{p,g}}}{dt} \right)_{\text{KH}} = 10^{-5} \left(\frac{M_{\text{p}}}{10 M_{\oplus}} \right)^4 \left(\frac{\kappa_{\text{env}}}{1 \text{ cm}^2 \text{ g}^{-1}} \right)^{-1} M_{\oplus} \text{ yr}^{-1} \quad (15)$$

where κ_{env} is the planet's gas envelope opacity. We assume $\kappa_{\text{env}} = 0.05 \text{ cm}^2 \text{ g}^{-1}$ and that it does not vary with metallicity, as in Liu et al. (2019).

Physically, the Kelvin-Helmholtz thermal contraction in Equation 15 promotes the envelope mass growth in the first place. As the planet grows, the accreted gas is further limited by the total amount entering the planetary Hill Sphere, adopted from Liu et al. (2019) below:

$$\left(\frac{dM_{\text{p,g}}}{dt} \right)_{\text{Hill}} = f_{\text{acc}} \nu_{\text{H}} R_{\text{H}} \Sigma_{\text{Hill}} = \frac{f_{\text{acc}}}{3\pi} \left(\frac{R_{\text{H}}}{H_{\text{g}}} \right)^2 \frac{\dot{M}_{\text{g}} \Sigma_{\text{gap}}}{\alpha_{\text{g}} \Sigma_{\text{g}}}. \quad (16)$$

where $\nu_{\text{H}} = R_{\text{H}} \Omega_{\text{K}}$ is the Hill velocity; $R_{\text{H}} = (M_{\text{p}}/3 M_{\star})^{1/3}$ is the Hill radius of the planet; and Σ_{Hill} is the gas surface density near the planet's Hill sphere. In this paper, we set $f_{\text{acc}} = 0.5$ to be the gas fraction that can be accreted by the planet's Hill sphere. Once the planet becomes sufficiently massive, accretion is dictated by the global disk gas inflow across the planetary orbit.

We adopt a combined migration formula by incorporating both type I and type II regimes (Kanagawa et al. 2018):

$$\dot{r} = f_{\text{tot}} \left(\frac{M_{\text{p}}}{M_{\star}} \right) \left(\frac{\Sigma_{\text{g}} r^2}{M_{\star}} \right) h_{\text{g}}^{-2} \nu_{\text{K}}, \quad (17)$$

and the migration coefficient is given by

$$f_{\text{tot}} = f_{\text{I}} f_{\text{s}} + f_{\text{II}} (1 - f_{\text{s}}) \frac{1}{\left(\frac{M_{\text{p}}}{M_{\text{gap}}} \right)^2}, \quad (18)$$

where M_{p} is the mass of the planet, ν_{K} is the Keplerian velocity and f_{I} and f_{II} correspond to the type I and II migration prefactors,

respectively. The type II migration coefficient $f_{\text{II}} = -1$ whereas the type I migration coefficient f_{I} sets the direction and strength of the type I torque, determined by the disk thermal structure and local turbulent viscosity α_{t} (Paardekooper et al. 2011). We choose the smooth function $f_{\text{s}}^{-1} = 1 + (M_{\text{p}}/M_{\text{gap}})^4$. This ensures that $\dot{r} \approx \dot{r}_{\text{I}}$ when $M_{\text{p}} \ll M_{\text{gap}}$ and $\dot{r} \approx \dot{r}_{\text{II}}/(M_{\text{p}}/M_{\text{gap}})^2$ when $M_{\text{p}} \gg M_{\text{gap}}$ (Kanagawa et al. 2018).

2.3 Stellar luminosity evolution

As a wholly convective star evolves along its Hayashi track until it develops a radiative core, the stellar luminosity evolves in response. The parameterization of the stellar luminosity evolution depends on stellar mass. Importantly, L_{\star} decreases with age for low-mass stars ($M_{\star} \leq 1.5 M_{\odot}$), but has an upward turn and remains high for more massive stars ($M_{\star} > 1.5 M_{\odot}$) due to their transition to the radiative regime (Palla & Stahler 1993; Siess et al. 2000; Baraffe et al. 2002). Furthermore, Johnston et al. (2025) found that giant planet formation is sensitive to the evolution of stellar luminosity, specifically the locations and times at which giant planet formation can occur depend on it. High stellar luminosity causes an increase in the scale height of the gas, which may decrease the efficiency of pebble accretion, making it more challenging to form giant planets (Johnston et al. 2025).

Thus in our model, we now adopt an evolving stellar luminosity derived from the evolutionary tracks in the Siess models (Siess et al. 2000). We select stellar luminosity values at timesteps 0.1–10 Myr with solar metallicity ($Z=0.01$) for stellar masses in the range of 0.9–5 M_{\odot} accounting for the majority of the stellar masses in the observational sample from Wolthoff et al. (2022) and interpolate the values in between.

We recognise that our model is limited by the sole X-ray photoevaporation prescription. This is due to X-ray rates being well-constrained whereas FUV photoevaporation rates are notoriously challenging to quantify due to FUV interacting with the dust. This regime switch typically occurs when stars become radiative (Kunitomo et al. 2021). Intermediate-mass stars become radiative early on in terms of disk lifetime (1–3 Myr), causing their X-ray rates to drop and FUV to become the dominant mass-loss mechanism (Kunitomo et al. 2021). While this is only a main concern for sampled stars in the range of 2.5–5 M_{\odot} , where the observed giant planet occurrence rate remains incredibly low (< 5%) (Reffert et al. 2015; Wolthoff et al. 2022), it is still important to consider in the context of our model. Our attempt to mitigate this is by having all our model embryos born at time 0.1 Myr - when X-rays are still the dominant photoevaporation mechanism for most of our stellar mass range.

3 MODEL ASSUMPTIONS

We carry out a population synthesis study, resulting in the final masses and locations of planets formed in our models. This allows us to explore the frequency and efficiency of planet formation with varying initial disk conditions, and to investigate the birth locations of embryos that grow into successful giant planets. The disk model is as described in Section 2.1. We proceed by conducting 100 numerical simulations for each stellar mass and metallicity combination from the Wolthoff et al. (2022) sample for the growth of a single embryo by Monte Carlo sampling each of the initial conditions: R_{d0} sampled between 20 and 200 AU, r_0 sampled logarithmically between 0.1 and 100 AU. The birth time is fixed at $t_0=0.1$ Myr and the pebble size $R_{\text{peb}}=1$ mm. The initial birth mass of the embryos is derived

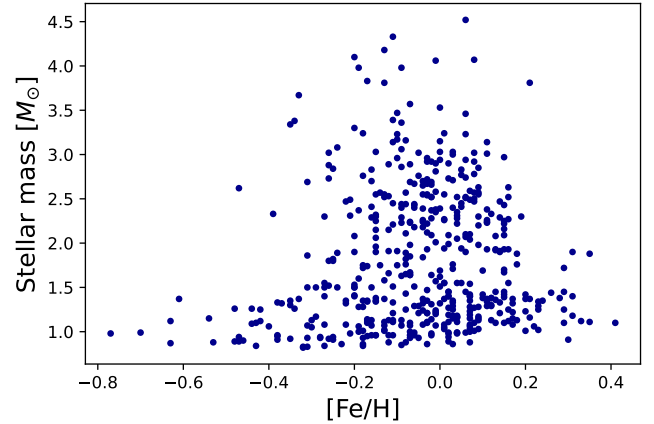


Figure 1. Stellar metallicity versus mass for the 482 stars of the homogenised combined RV sample (Wolthoff et al. 2022).

from Equation 8. We use the stellar masses and metallicities from the homogenised stellar sample in Wolthoff et al. (2022) (described below). The adopted distributions of disk and stellar parameters are summarised in Table 1. These parameters are discussed in more detail below.

3.1 Stellar sample

For our analysis, we use the homogenised stellar sample in Wolthoff et al. (2022), which is comprised of 482 stars (see Figure 1). This combines observations from three RV surveys: the Lick giant star survey (Reffert et al. 2006); the EXo-Planets aRound Evolved StarS (EXPRESS) survey (Jones et al. 2011); and the Pan-Pacific Planet Search (PPPS) (Wittenmyer et al. 2011). This sample accounts for partial target overlaps of the three surveys (EXPRESS and PPPS surveys have 37 stars in common; Lick and EXPRESS share 12 stars; and Lick and PPPS overlap with one star) and contains only single star systems.

The stellar parameters (mass, radius, age, surface gravity, effective temperature, and luminosity) for the extended sample were homogeneously derived by Wolthoff et al. (2022) using the method of Stock et al. (2018), which uses Bayesian inference to compare spectroscopic, photometric, and astrometric observables to the PARSEC evolutionary tracks (Bressan et al. 2012), incorporating evolutionary timescales and the initial mass function as priors. For each stellar parameter, two probability distribution functions are generated: one assuming the star is ascending the red-giant branch (RGB), and one assuming it has reached the horizontal branch (HB), each with an associated probability. Wolthoff et al. (2022) adopt the stellar parameters corresponding to the most probable evolutionary stage.

Concerns have been raised in the literature about the systematic overestimation of stellar masses (Lloyd 2011, 2013; Schlaufman & Winn 2013). However, several studies found no evidence for a significant systematic discrepancy (Johnson et al. 2013; Ghezzi & Johnson 2015; North et al. 2017; Ghezzi et al. 2018). The method of Stock et al. (2018) is robust in this regard, as it explicitly accounts for evolutionary timescales, the initial mass function, and the two distinct evolutionary stages separately.

3.2 Accretion rate

Mass accretion rate is one of the most important factors in any kind of planet formation simulations. It governs the rate of dust and gas fall onto the central star (and hence disk lifetime) as well as how efficiently pebble accretion can proceed. It is especially important in the case of giant planet formation as the accretion rate must be high enough in order for planets to grow massive before the disk material is dissipated through photoevaporation processes (Liu et al. 2019; Johnston et al. 2024).

Figure 2 is adapted from the Appendix of Iglesias et al. (2023) and shows the mass accretion rates for the Herbig Ae/Be stars in Wichittanakom et al. (2020); Iglesias et al. (2023), along with the sample of low-mass stars in the Chamaeleon I star-forming region studied in Manara et al. (2017). The highlighted region shows our stellar mass range of interest. The best linear fits for each sample is shown, derived over their respective full mass ranges: M17 refers to the fit derived from Manara et al. (2017); W20 to that from Wichittanakom et al. (2020); and J24 to our own estimate as described below. When we are conducting our planet population synthesis, we use the recorded stellar masses from our sample in Figure 1 (Wolthoff et al. 2022), and select the corresponding accretion rate \dot{M}_{acc} from the linear fit in Figure 2 and use that as the initial accretion rate \dot{M}_{g0} at $t=0$ Myr in Equation 1 for our model.

Furthermore, we consider the ages of the stars in Figure 2, where the colour of the data is associated with the stellar age in Myr. There are no individual ages for the low-mass stars in the Manara et al. (2017) sample so we instead adopt the age of the Chamaeleon I star-forming region to be 1.5 Myr (Galli et al. 2021). The ages for the Herbig Ae/Be stars in Wichittanakom et al. (2020) are either derived from the same study or from Vioque et al. (2018). The highlighted region again denotes our stellar mass range of interest for this study. The majority of the Manara et al. (2017) low-mass stars, alongside the very young and massive Herbig Ae/Be stars in the Wichittanakom et al. (2020) sample, are beyond our stellar mass range of interest.

The stars with masses that do lie in our range of interest are mainly Herbig Ae/Be stars in the Iglesias et al. (2023) and a part of the Wichittanakom et al. (2020) sample. Such stars vary in age from 1–20 Myr, with only a few of the most massive stars having ages reported below 1 Myr. This diversity in the age of these stars provides an interesting challenge for us given that accretion rates decay over time, typically beginning to drop substantially anywhere between 1–2 Myr for 1–2.4 M_{\odot} stars (Johnston et al. 2024). This motivates our adoption of the J24 prescription as the observed values may be an underestimation of the initial \dot{M} if the accretion rates of these stars have been dropping for several Myr.

3.3 Disk mass

As in Pascucci et al. (2016), we assume the disk mass to be super-linearly correlated with the mass of the host star. This is determined by dust continuum emission measurements with ALMA (Pascucci et al. 2016; Manara et al. 2016). In particular, Manara et al. (2016) combined results of surveys from VLT/X-shooter and ALMA to find a correlation between the mass accretion rate and the disk dust mass, confirming that mass accretion rates are related to the properties of the outer disk. In our model, the disk evolves viscously in tandem with the mass accretion rate (\dot{M}_g) onto the central star and is correlated with the mass of the disk (M_d) (Hartmann 1998). Hence, the ratio between \dot{M}_g and M_d can be expressed as the viscous timescale at the outer edge of the disk (Liu et al. 2019):

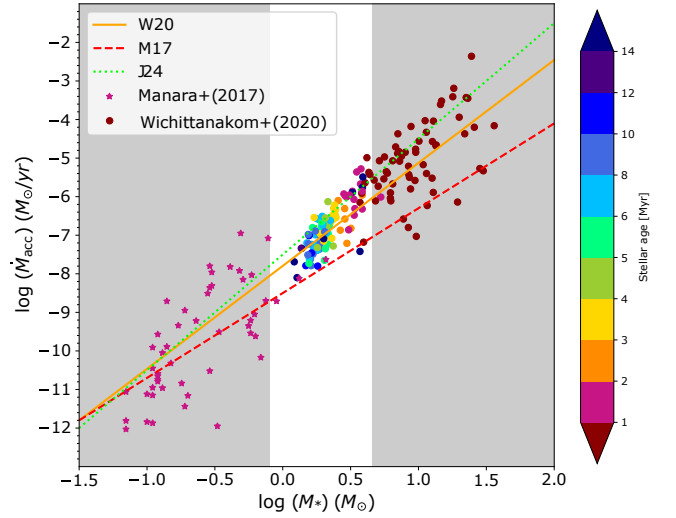


Figure 2. Mass accretion rates from observational studies (Wichittanakom et al. 2020; Manara et al. 2018), adapted from the Appendix of (Iglesias et al. 2023). Linear fits are shown for reference; dashed red line for M17, dotted line for J24, and solid orange line for W20. The stars are colour coded by stellar age. There are no individual ages for stars in the sample by (Manara et al. 2017), so we adopt the age of the Chamaeleon I star-forming region to be 1.5 Myr from (Galli et al. 2021). The white highlighted region is the stellar mass range that we are interested in exploring.

$$t_{\text{vis}} = \frac{1}{3(2+s)^2} \frac{r_{d0}^2}{\nu_0}. \quad (19)$$

r_{d0}^2 and ν_0 are the initial characteristic size of the gas disk and the viscosity at that radius, and s is the gas surface density gradient. Notably, the viscosity is dependent on sound speed (c_s), scale height of the gas disk (H_g), and Keplerian angular frequency (Ω_K), as defined above. These terms have M_{\star} - and L_{\star} -dependence, meaning that the viscous timescale evolves differently around host stars of different masses.

Initial characteristic disk size - R_{d0} - is the corresponding length scale for viscous disk evolution (Liu et al. 2019). Bate (2018) performed sophisticated radiation hydrodynamical simulations of star formation in clusters. Their results indicated that the sizes of the early protostellar disks are poorly (or at most weakly) dependent on M_{\star} . As such, we assume that R_{d0} has no correlation with M_{\star} . Instead, we allow R_{d0} to be sampled uniformly between 20–200 au.

3.4 Birth location and birth embryo mass

The birth location of the embryo is randomly sampled between 0.1–100 au. This has important consequences for the initial birth mass of the embryo as we adopt our streaming instability condition, as defined in Equation 8.

Figure 3 demonstrates the initial birth mass of embryos at 0.1 Myr in disks around stars of masses 1, 1.7, and 2.4 M_{\odot} . Within the first few au, the birth masses are essentially identical regardless of stellar mass. These stellar masses are illustrative but correspond to the rise, peak, and fall of the observed occurrence rate. In this mass range, the stars remain wholly convective (*i.e.* dominated by X-ray photoevaporation) for the times taken for giant planet formation to conclude in our models. At birth locations beyond 3 au, the birth masses begin to diverge, with the largest birth masses corresponding

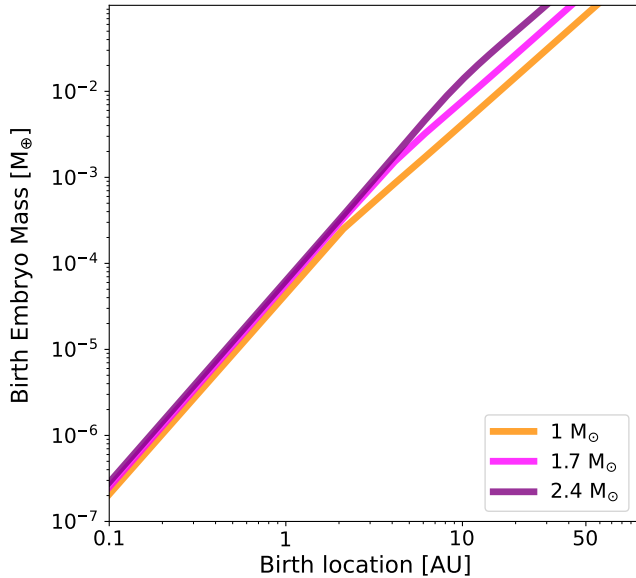


Figure 3. Birth location against birth embryo mass for time 0 for key stellar masses 1 (orange), 1.7 (pink), and 2.4 M_{\odot} (purple). Within the first few au of the host stars, the birth embryo masses are essentially identical.

to the most massive stars. This in turn impacts the rate of pebble accretion (Equations 10 & 11) and subsequently dictates when/if runaway gas accretion can proceed.

3.5 Birth time

We set the birth time for all embryos to be 0.1 Myr. While Johnston et al. (2024) found that giant planet formation can proceed up to 3 Myr under the most favourable conditions, we fix the embryo formation time to the earliest epoch in order to circumnavigate the limitation of our model: we employ only an X-ray photoevaporation prescription, despite our evolving PMS (Section 2.3). We do not model the transition in photoevaporation mechanism from X-ray to FUV (Kunitomo et al. 2021), which occurs when a convective star becomes radiative. The radiative core develops radiative core. For stars less massive than 2.5 M_{\odot} , - the range corresponding to the rise, peak, and fall of the giant planet occurrence rate as a function of stellar mass - disks are still primarily dispersed by X-ray photoevaporation (Kunitomo et al. 2021). Additionally, the photospheres of stars less massive than 1.6 M_{\odot} never become hot enough to emit FUV (Kunitomo et al. 2021). By fixing $t_0 = 0.1$ Myr, our embryos are formed when X-rays remain the dominant mechanism across most of our stellar mass range.

4 GIANT PLANET OCCURRENCE RATE AS A FUNCTION OF STELLAR MASS AND METALLICITY

One of the most striking results from Reffert et al. (2015) was the steep decline in the giant planet occurrence rate for stellar masses greater than 2.5–3 M_{\odot} . Of the 113 stars examined, no confirmed giant planets were found around stars more massive than 2.7 M_{\odot} . Thus, their planet occurrence rate for stars in the range of 2.7–5 M_{\odot} was found to be $0.0^{+1.6}_{-0.0}\%$ (Reffert et al. 2015). This complements earlier works which found an increase in the occurrence rates of giant

Parameter	Description
disk model	viscously heated + stellar irradiation
M_{\star} [M_{\odot}]	Figure 1 sample (0.82–4.52)
Z_{\star} [Fe/H]	Figure 1 sample (−0.77–0.41)
\dot{M}_{g0} [$M_{\odot} \text{ yr}^{-1}$]	Derived from Figure 2. J24: $y=3x - 7.7$ W20: $y=2.67x - 7.8$; M17: $y=2.2x - 8.8$
R_{d0} [AU]	U(20, 200)
r_0 [AU]	log U(0.1, 100)
t_0 [Myr]	0.1
R_{peb} [mm]	1
M_{p0} [M_{\oplus}]	Eq. (8), Figure 3

Table 1. Adopted parameter distributions for the population synthesis study.

planets with M_{\star} , but only exploring up to 2 M_{\odot} (Johnson et al. 2010; Bowler et al. 2010).

Wolthoff et al. (2022) repeated the same process by combining data from the Lick, EXPRESS, and PPPS giant star RV surveys. This sample consisted of 482 stars hosting 37 giant planets in 32 systems, with planetary masses in the range of 0.8–24.4 M_{Jup} . The majority of these planets were concentrated at higher metallicities and stellar masses between 1–2 M_{\odot} , with no planet-hosting stars more massive than 3 M_{\odot} (Wolthoff et al. 2022). They also found a distinct peak in the giant planet occurrence rate above 1.5 M_{\odot} with an exponential drop for stars more massive than 1.8 M_{\odot} , consistent with Reffert et al. (2015); Jones et al. (2015). During their Bayesian fitting, they found the maximum planet occurrence rate is reached at $M_{\star}=1.7 M_{\odot}$.

Taking selection biases and observational sensitivity into account, Wolthoff et al. (2022) then fit the giant planet occurrence rate as a function of stellar mass and metallicity with a Gaussian and exponential fit, respectively. The Gaussian plus exponential distribution has the following form with the model parameters $X = (C, \mu, \sigma, \beta)$:

$$f(M_{\star}, [\text{Fe}/\text{H}]) = C \exp\left(-\frac{1}{2} \left[\frac{M_{\star} - \mu}{\sigma}\right]^2\right) 10^{\beta[\text{Fe}/\text{H}]}, \quad (20)$$

where the maximum likelihood values from Wolthoff et al. (2022) are: $C=0.128 \pm 0.027$, $\mu=1.68 \pm 0.59 M_{\odot}$, $\sigma=0.70 \pm 1.02 M_{\odot}$, and $\beta=1.38 \pm 0.36$.

4.1 Dependence of the giant planet occurrence rate on the accretion rate

We will now examine the results of giant planet occurrence rate in relation to the stellar mass and metallicity in detail. We do this by counting the number of giants produced from our population synthesis per stellar mass/metallicity combination corresponding to the values from our RV sample in Figure 1 from Wolthoff et al. (2022). We do this for each of our stellar mass-accretion rate relations outlined in Figure 2 (M17, W20, and J24), such that we can examine the importance of the mass accretion rate in modelling the observed giant planet rate as a function of stellar mass.

In Figure 4, planet occurrence rates are colour-coded according to the bar on the right hand side of the plots. The blank areas of the diagrams correspond to metallicity/mass combinations with no existing measurements in the observational sample (Figure 1).

Figure 4 shows the planet occurrence heat maps from our models alongside the observed giant planet occurrence rate for the Lick stars (which accounts for the majority of our stellar sample) adapted from

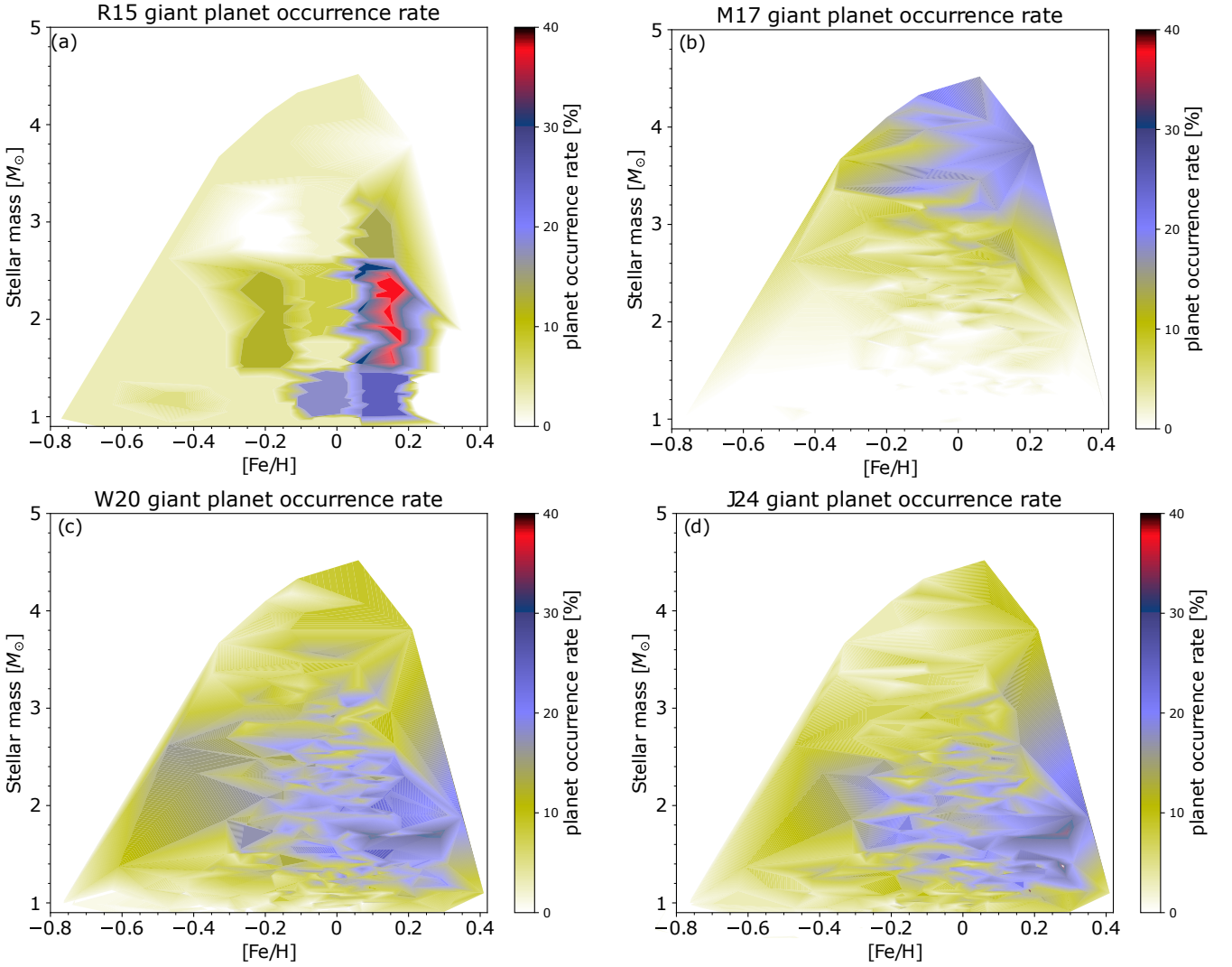


Figure 4. Planet occurrence rate (colour coded) as a function of metallicity and stellar mass in the *Lick* stars in our sample (Reffert et al. 2006; Wolthoff et al. 2022) (a) and in our synthetic models: M17 (b), W20 (c), and J24 (d). Data has been adapted from (Reffert et al. 2015) and heavily smoothed in (a) so that general trend can be examined. There is a clear maximum in the observed planet occurrence rate (a) for metallicities of about 0.2 and masses of about $2 M_{\odot}$. For our models (b, c, d), the peak of planet formation shifts depending on the initial conditions and is more concentrated as the data does not need to be smoothed.

Fig. 2 and Fig. 3 in Reffert et al. (2015). It shows a clear peak in the giant planet rate for high metallicities of ~ 0.2 dex and stellar masses around $\sim 2 M_{\odot}$.

Figure 4b shows the heat map for the planet occurrence rate for the M17 accretion rates shown in Figure 2. The occurrence rate of giant planets very clearly increases with increasing stellar mass and metallicity. Occurrence rates $\geq 20\%$ are only possible when the stellar mass is $\geq 3 M_{\odot}$, which is clearly at odds with the observational peak of $M_{\star} \sim 1.7 M_{\odot}$ calculated in Wolthoff et al. (2022).

For our W20 model in Figure 4c, we see that the mass/metallicity combinations required for high occurrence rates are very different than in Figure 4b. The occurrence rates of around 20% (blue) are now found at stellar masses $\leq 2.5 M_{\odot}$ and metallicities between -0.2 – 0.2 . There is some evidence of giant planet occurrence rates of 20% (blue) up to $3 M_{\odot}$ for only high metallicities. The peak of giant planet occurrence distribution (more than 30%, dark blue) now occurs around stellar mass of $1.7 M_{\odot}$ and metallicities 0 – 0.2 . Our modelled planet rates are similar to that of the observational

occurrence rates in Reffert et al. (2015) (Figure 4a). W20 produces lower occurrence rates than R15 in some bins, which we attribute to the smaller sample size of R15 leading to elevated rates in individual bins due to small-number statistics. However, both W20 and R15 are in agreement that the highest rates of giant planets are found in systems with $M_{\star} = 1.5 - 2 M_{\odot}$ and metallicity ~ 0.2 dex.

Finally, we consider our J24 model of giant planet rate in Figure 4d. Overall, it is broadly similar to both the W20 model and the R15 planet rate, albeit more concentrated in the region of high metallicities and stellar masses ~ 1.6 – $1.8 M_{\odot}$.

As discussed in Section 3.2, the M17 fit is the best fit for the low-mass T Tauri stars in the (Manara et al. 2017) sample. Given that the majority of our stellar mass sample from Wolthoff et al. (2022) are more massive than $1 M_{\odot}$, this results in the accretion rates for our model systems to be lower than one might observe in low-mass stars. Furthermore, when we consider the ages of the stars in the mass accretion rate observations in Figure 2, it is clear that this accretion rate fit M17 is not representative of accretion rates

for stars with advance ages (≥ 10 Myr) for the upper end of stellar masses in our sample. The consequence of these low observed initial accretion rates around more massive stars is the prolonging of the protoplanetary disk lifetime. This results in the model giant planet occurrence rate being skewed to higher stellar masses because there is a weaker limiting factor of the disk lifetime in such systems.

Concurrently, there are extremely low giant planet occurrence rates when the stellar masses are less than $2 M_{\odot}$. Again, a consequence of the very low accretion rates from the less massive stars in our sample. While the disks around stars less massive than $2 M_{\odot}$ likely survive for a long time, the gas accretion is so low that pebble accretion (Equation 10) becomes incredibly inefficient. Many of the planets in such systems would not be able to accrete enough solid material to undergo runaway gas accretion. This is further exacerbated by our assumption within the planet formation model that the disk mass is correlated with the mass accretion rate (described in Section 3.3). Hence we can conclude that this particular model setup is not a good match for the observed giant planet occurrence rate and do not include in further analysis.

The W20 and J24 models have initial accretion rates are much higher than the M17 fit overall. This impacts where the peak of the giant planet occurrence rate occurs: (i) for less massive stars, the higher accretion rates improves the rate of pebble accretion so they can surpass pebble isolation mass to undergo runaway gas accretion at earlier times and (ii) for more massive stars, the very high accretion rates aids in fast disk evolution which suppresses the timeframe for giant planet assembly.

To conclude, the final planet occurrence rate is very sensitive to the accretion relation, and thus stellar-mass dependent accretion rates are vital to giant planet formation. There is a balance to be struck between efficient pebble accretion and dissipating the disk too quickly. We explore this balance further below.

4.2 Giant planet dependence on M_{\star} and Fe/H

In Figure 5, we show the mean model giant planet occurrence rate as a function of stellar mass (left) and metallicity (right). Our mean-averaged results for for the W20 and J24 models, derived using the same binning process, are shown in orange and lime respectively.

When binned as a function of stellar mass in Figure 5 (left), we can see that our W20 model follows a broadly similar shape to the observed planet rate. The peak of our model planet distribution is found when the mean stellar mass bin is $M_{\star}=1.87 M_{\odot}$. Overall, the giant planet occurrence rate reaches $\eta_{\text{J}} \sim 19\%$ for stars in the range of $1.6\text{--}2.15 M_{\odot}$. There is a slow decline in the planet rate for stellar masses $M_{\star} > 2.15 M_{\odot}$ which drops off more steeply when $M_{\star} > 2.5 M_{\odot}$. Although consistent with the observational findings of a distinct peak in the occurrence rate for stars more massive than $1.5 M_{\odot}$ (Reffert et al. 2015; Jones et al. 2015; Wolthoff et al. 2022), our drop-off in stars more massive than $M_{\star} > 2.5 M_{\odot}$ is not quite as steep as the observed results. Our planet occurrence rate remains above 5% for even the most massive stars in our sample. This can be explained in three main ways.

Firstly, that our model is an idealised system - a wholly smooth disk with only a single planet being formed in each iteration of our simulation. Thus, there are no rings, gaps, discontinuities, or other growing planets competing for material. Additionally, we are working under the assumption that giant planets are always formed via core accretion and disregard the possibility of disk fragmentation. However, Cadman et al. (2020) found that disks around stars more massive than $2 M_{\odot}$ are more susceptible to gravitational instability and disk fragmentation.

Secondly, while we implement PMS stellar evolution, as detailed in Section 2.3, we solely model photoevaporation via X-rays and do not include a shift in the dominant photoevaporation mechanism to FUV, corresponding to convective stars becoming radiative. Stars $\leq 2.5 M_{\odot}$ mainly disperse via X-ray photoevaporation, but stars between $1.7\text{--}2.5 M_{\odot}$ do become radiative and therefore hot enough for FUV to dominate on a timescale of around $5\text{--}8$ Myr that decreases with increasing stellar mass (Kunitomo et al. 2021). Stars more massive than $3 M_{\odot}$ are hot enough to have a radiative core from the beginning (Kunitomo et al. 2021). Kunitomo et al. (2021) found that FUV is the main mechanism behind disk dispersal in stars more massive than $3 M_{\odot}$. Depending on how efficient FUV photoevaporation is at dispersing dust and gas in the disk, this could affect how many giant planets are able to form before limited material prohibits it. Consequently, this could decrease the number of giants found in our model when $M_{\star} > 2.5 M_{\odot}$. In the context of the observational results, this might indicate that FUV is effective at removing material to cause such a low planet rate around stars more massive than $3 M_{\odot}$.

Thirdly, our results may also reflect the age bias in observational accretion rates in Figure 2. As discussed in Section 3.2, we may be underestimating the accretion rate of these stars by using them as the initial accretion rate assumption for our W20 model at 0.1 Myr. For stars less massive than $1.25 M_{\odot}$ in Figure 5 (left), it gives a fairly good prediction for the rise of the giant planet occurrence rate within this stellar mass range. But as detailed above, the 'peak' of our model distribution spans $M_{\star}=1.8\text{--}2.15 M_{\odot}$, shifted slightly towards more massive stars than the observed peak. Thus, it may be prudent for us to make our own estimation for this age discrepancy (J24).

To summarise, our W20 model gives a good approximation of the overall rise, peak, and fall of the giant planet occurrence rate as a function of stellar mass. The overestimation of the planet rate can likely be attributed to the physical limitations of our model discussed above. The broadness of the peak and the slow drop off for stars more massive than $2.5 M_{\odot}$ may be due to the age bias present within our accretion rate estimations (Figure 2). This leads us to explore our own estimation for the accretion rate, J24.

Examining our J24 occurrence rate as a function of stellar mass in Figure 5 (left), we can see that it provides a better fit to the observed and corrected occurrence rate than our W20 model. Specifically, we see a sharper rise in the planet rate up to $1.5 M_{\odot}$ and a steeper decline for stars more massive than $2 M_{\odot}$. Now, our model rates lie - for the most part - within the limits of the corrected occurrence rate.

Adopting stellar-mass dependent accretion rates that account for the age bias in the observed accretion rate data (Figure 2) has narrowed and shifted the peak of the giant planet rate in our J24 model to better reflect the observational results. The decline in the giant planet rate now falls off more quickly for stars more massive than $1.5 M_{\odot}$ due to the higher accretion rates aiding in fast disk evolution and thus reducing the number of successful giant planets. At the low end of our stellar mass range, there is a balance to be found: the accretion rate must be high enough to drive efficient pebble and gas accretion, yet not so high as to disperse the disk before a giant planet can form. Observationally, this balance appears to be optimised around $1.7 M_{\odot}$ (Wolthoff et al. 2022).

Now, when binned as a function of metallicity in Figure 5 (right), we can see that the planet rate in both of our models (W20 and J24) increases with increasing metallicity up to 0.3 [dex]. Beyond this, we especially suffer from small number statistics which accounts for the low rates at this limit. The J24 model produces a higher rate of giant planets for larger metallicities than our W20 model, likely due to the overall higher accretion rates in the J24 model which in turn helps aid the rate of pebble accretion.

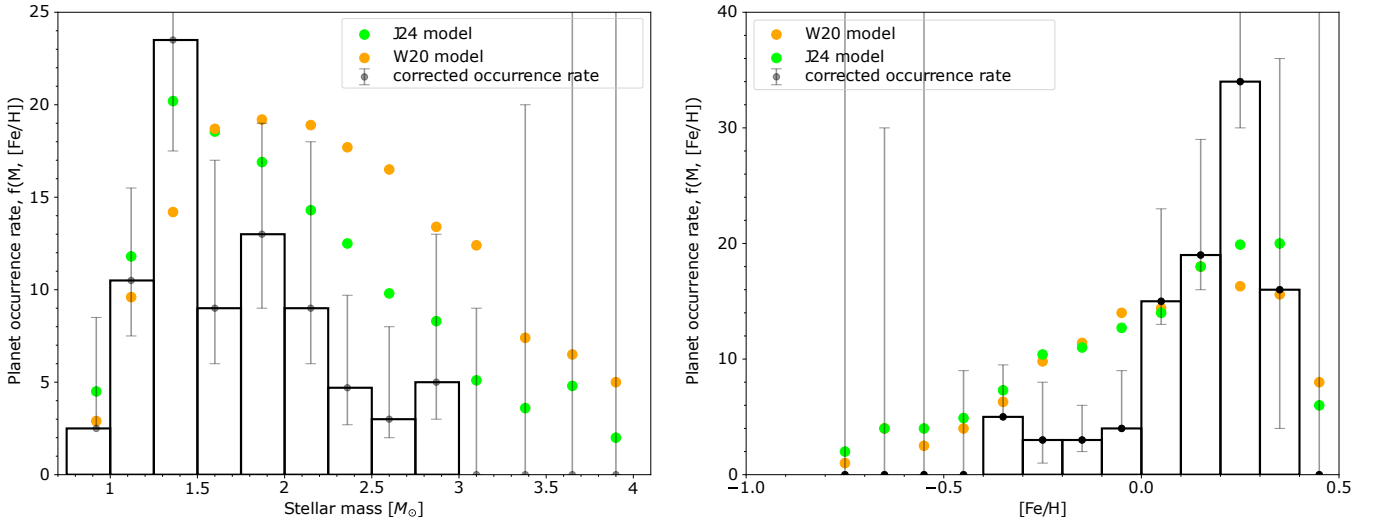


Figure 5. Histogram of our mean model giant planet occurrence rates as a function of stellar mass (left) and metallicity (right). Our best mean models are coloured in orange (W20) and lime (J24), respectively. The solid black histograms shows the completeness-corrected observed giant planet occurrence rate in each bin (Wolthoff et al. 2022).

Within our models, metallicity is represented by the dust-to-gas ratio. A larger metallicity means a higher ratio of solids to gas within our disks which enhances the pebble growth. This allows the planetary embryos to grow more massive at a faster rate, meaning that a higher proportion of embryos can surpass isolation mass at an early enough stage to accrete enough gaseous material to become a giant planet. This results in an increased giant planet occurrence rate for higher metallicities, as seen in Figure 5 (right). Overall, both of our models are in agreement with previous observational studies that found a positive planet-metallicity correlation (Hekker & Meléndez 2007).

5 GIANT PLANET POPULATION PROPERTIES

In this section, we explore the properties of the giant planets formed in our population synthesis models W20 and J24. Namely: the final planetary masses, and the times and locations where these giant planets accumulate the bulk of their mass through runaway gas accretion. These locations present starting points for subsequent inward migration, as long as the gas disc is sustained (Kanagawa et al. 2018). We investigate how these properties relate to the stellar mass.

5.1 Location and time of runaway gas accretion

Figure 6 shows the mean times and locations where our giant planet population accumulates the bulk of its mass during the runaway gas accretion phase as a function of stellar mass. The black diamonds are the 37 confirmed giant planets from the Wolthoff et al. (2022) sample - described in Section 3.1. For both our W20 (orange) and J24 (lime) synthetic planet populations, clear trends are visible.

Giant planets form earlier around more massive stars. At $1 M_{\odot}$, it takes around 1 Myr to grow a giant planet on average and this mean timescale has reduced to just 0.5 Myr by $4 M_{\odot}$. This trend follows directly from the stellar-mass dependent accretion rates discussed above. High accretion rates - coupled with shortened disk lifetime and an enhanced rate of pebble accretion - mean that giant planets in such systems must form rapidly in order to exist at all. The increasing \dot{M}_{g} with stellar mass corresponds to a higher solid accretion rate onto

the planetary core (Equation 10). Therefore, even though pebble isolation mass (Equation 13) scales with stellar mass, some embryos are able to accumulate enough solid mass very quickly when the gas and solid accretion rates are at their highest.

This is reflected further in the giant planet location plot of Figure 6: the orbital location where giant planets accumulate the bulk of their mass increases with stellar mass, reaching ≥ 10 au for stars more massive than $\sim 2.5 M_{\odot}$. Around low-mass stars the disk persists for longer, allowing giant planets to grow at a slower pace and complete runaway gas accretion within ≤ 5 au. Around more massive stars, the rapidly dispersing disk means that runaway gas accretion must occur at larger orbital radii before the available gas is removed.

A critical point regarding Figure 6 is that the simulated locations are *not* the final orbital positions - they are the radii at which runaway gas accretion occurs, *i.e.* the starting points for subsequent migration. The observed giant planets (black diamonds) are all found within ≤ 5 au, consistent with their having undergone substantial inward migration after the runaway gas accretion phase. Indeed, the large offset between the simulated accretion locations (5–20 au) and the observed orbital radii (≤ 5 au) implies that significant inward migration is expected in all cases. This is physically plausible: as long as the disk retains sufficient gas after the runaway accretion phase, migration will drive the planet inward on a timescale comparable to the local viscous timescale (Kanagawa et al. 2018). Since our model forms giant planets at early times ≤ 1 Myr, upper panels of Figure 6), there is substantial disk material remaining to facilitate this inward migration. This also provides a natural explanation for why our occurrence rates in Figure 5 can match observations despite the apparent discrepancy in locations: the simulated planets are not stranded at their formation radii, and migration brings them into the detectable range of RV surveys.

That said, this migration is not guaranteed to be complete for all simulated planets, nor is it uniform. Planets forming at the largest radii - particularly those around stars more massive than $\sim 2.5 M_{\odot}$ - may not migrate sufficiently far inward within the remaining disk lifetime to be detectable by RV surveys, which are generally sensitive to planets within ≤ 5 au. This suggests that some fraction of our simulated giant planets at large radii around massive stars would *not*

be counted in the observed sample, which could contribute to the marginal overproduction of giant planets in our W20 model at high stellar masses in Figure 5. A quantitative treatment of post-formation migration and its detectability is beyond the scope of this work, but represents an important avenue for future modelling. However, an important impediment is presented by engulfment of the innermost planets at later stages of stellar evolution (Kunitomo et al. 2011).

We note that the gap between the simulated accretion locations (coloured circles) and the observed orbital radii (black diamonds) in the lower panels of Figure 6 can itself be interpreted as an observationally interesting parameter space. The region between $\sim 5\text{--}15$ au around intermediate-mass stars ($1.5\text{--}3 M_{\odot}$) corresponds to where giant planets in our model are born, and where some fraction of them may remain if migration is halted early. For example, by the dissipation of the disk, or by trapping at a local pressure maximum (Kanagawa et al. 2018). This wide-orbit population would be largely inaccessible to current RV surveys, and the brightness of intermediate-mass host stars renders direct imaging at these separations extremely challenging due to the unfavourable contrast ratio (Nielsen et al. 2019; Wagner et al. 2019). Astrometric surveys - in particular those enabled by *Gaia* and its successors - are therefore the most promising avenue for probing this parameter space and constraining what fraction of giant planets remain on wide orbits rather than migrating inward.

The large orbital radii at which giant planets around more massive stars undergo runaway gas accretion also has implications for their atmospheric composition. At such distances, H_2O and CO_2 are locked in the ice phase, while CO remains in the gas phase. Any gas accreted in such a regime would be CO -rich, potentially producing a super-stellar C/O ratio in the planetary atmosphere. In hot ($T \gtrsim 1200$ K) photospheres, the H_2O abundance is sensitive to both the O/H and C/O ratios (Welbanks et al. 2019). A super-stellar C/O ratio can suppress the H_2O abundance and produce giant planets that are metal-rich but oxygen-poor (Madhusudhan et al. 2014; Welbanks et al. 2019).

Figure 6 includes only the mean-averaged values per stellar mass bin, and we note that small-number statistics affect the robustness of these averages at both ends of the stellar mass range, where our model giant planet rates fall below 5% (Figure 5, left). Additional observational detections at these limits would help constrain these trends. Nevertheless, since core accretion is thought to be the dominant giant planet formation mechanism (Pollack et al. 1996), our model could be extended to incorporate disk structures such as rings and pressure bumps that could locally halt migration and retain planets on wider orbits. Additionally, a more complete treatment of photoevaporation across the full stellar mass range would be beneficial.

Overall, the accretion rate is a key parameter in determining the distribution of giant planets. The assumption of high accretion rates in the W20 and J24 models produces results consistent with current observational trends, supporting the hypothesis that (i) giant planet formation is dictated by the initial accretion rate and (ii) the orbital location of giant planets is largely dependent on the birth conditions of the natal disk.

6 SUMMARY AND CONCLUSIONS

We have presented a planet population synthesis study of giant planet formation across a range of stellar masses and metallicities, using the pebble-driven core accretion model of Liu et al. (2019), as adapted in Johnston et al. (2024, 2025). We choose the initial conditions of planet formation such that they are close to current observational

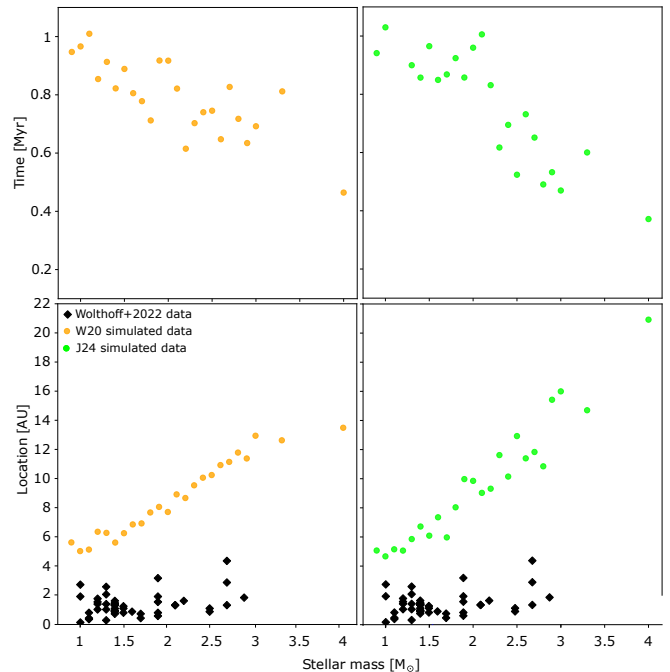


Figure 6. Mean giant planet properties as a correlation of M_{\star} of our planet population synthesis models W20 (orange) and J24 (lime). The black diamonds are the 37 confirmed giant planets from the (Wolthoff et al. 2022) sample. Time and location refer to when and where our synthesised giant planets accumulate the bulk of their mass to surpass $300 M_{\oplus}$.

trends. We investigate three different best fits for the observational accretion rate; (i) M17 for the low-mass stars in Manara et al. (2017); (ii) W20 for the intermediate-mass stars in Wichittanakom et al. (2020); and J24 as our own estimation to account for the wide range of ages present in the Wichittanakom et al. (2020) sample.

We find that by adopting observational stellar mass-dependent accretion rates (J24, Figure 2); disk lifetimes (Equation 2); and PMS stellar evolution (Section 2.3), we can produce giant planet rates as functions of stellar mass and metallicity that corresponds to the observed distribution in Wolthoff et al. (2022) (Figure 5). Furthermore, it is evident that our giant planet population models are highly sensitive to the initial accretion rate (Figures 4 & 5). When we adopt the observed low accretion rates around less massive stars, the low accretion rates suppress the efficient pebble growth and gas accretion required to form giant planets. Conversely, when we adopt the observed high accretion rates around more massive stars, the disk is dissipated at a faster rate which results in the embryos being quickly swept to the edge of the inner disk and hence preventing the growth of giant planets. This gives rise to the peak of occurrence rate around $1.75 M_{\odot}$, as derived observationally.

As a consequence of adopting this stellar-mass dependent accretion rate, we find that giant planets around more massive stars form at earlier times than around less massive stars, which counteracts the fast-acting disk dissipation (Figure 6). Additionally, these giant planets around more massive stars tend to accrete the bulk of their mass at greater distances from their host stars, allowing sufficient time for the core to acquire enough solid mass needed for the runaway gas accretion, before reaching the edge of the inner disk (Figure 6).

Our results from Figure 6 indicate that giant planets can form at a range of radii, including well beyond the H_2O snowline, without requiring icy grain enhancement of solid accretion. In fact, many of our successful giant planets are born well beyond the H_2O snowline.

This notably changes the classical view of giant planet formation via core accretion that often relies on the enhanced sticking efficiency of icy grains beyond the snowline to accelerate planetesimal and core growth. Instead, the stellar-mass dependent accretion rate alone appears sufficient to drive efficient core growth across a range of disk radii, in the context of pebble accretion driven planet formation models.

We also find that both our J24 and W20 models provide a reasonable agreement with the observed giant planet properties. This reaffirms our findings that accretion rate is the most important parameter in dictating whether giant planets can form in a system. Additionally, it provides an exciting avenue for future work: if we can successfully model the earliest stage of planet formation (*i.e.* giant planets), we can explore terrestrial planet formation from the remaining disk material and investigate the resulting planetary system architecture through dynamical modelling.

Moreover, future exoplanet observations - not only using radial velocity but astrometric methods such as those enabled by *Gaia* and forthcoming missions - have the potential to substantially improve our understanding of giant planet occurrence rates in the parameter space most relevant to giant planet formation and migration. As illustrated in Figure 6, the region between the simulated run-away accretion locations (5–20 au) and the currently observed orbital radii ($\lesssim 5$ au) represents a largely unexplored parameter space for intermediate-mass host stars. Astrometric surveys are particularly well-suited to probing this regime and would provide direct observational constraints on whether giant planets formed at large orbital radii subsequently migrate inward, remain on wide orbits, or are dispersed entirely. Each outcome carrying distinct implications for the giant planet occurrence rates discussed in this work.

Finally, our current model is limited by several assumptions which could explain our marginal overproduction of giant planets in Figure 5. Specifically, our assumption of a radially smooth disk neglects structures such as rings and gaps that could locally inhibit migration. In reality, the planets could be stopped at larger orbits by processes not included in our model. Furthermore, planets may have been removed in some stars due to engulfment during later stages of evolution. In future work, we hope to introduce some rings or gaps that would naturally inhibit planetary growth and migration. In conjunction with this, adopting a disk chemistry model would also allow us to find any chemical composition distinctions that may exist in the giant planet population, either as a function of stellar mass or metallicity.

ACKNOWLEDGEMENTS

This work was undertaken on ARC4, part of the High Performance Computing facilities at the University of Leeds, UK. We thank both Richard Booth and Daniela Iglesias for their helpful inputs. HFJ was supported by a Royal Society Grant (RF-ERE-221025) and the Science and Technology Facilities Council (Project Reference: 2441776). OP acknowledges support from the Science and Technology Facilities Council, grant numbers ST/T000287/1, and ST/X001016/1. BL is supported by National Key R&D Program of China (2024YFA1611803), National Natural Science Foundation of China (Nos. 12222303 and 12173035), the start-up grant of the Bairen program from Zhejiang University.

DATA AVAILABILITY

The data underlying this article will be shared on reasonable requests to the corresponding author.

REFERENCES

- Abod C. P., Simon J. B., Li R., Armitage P. J., Youdin A. N., Kretke K. A., 2019, *The Astrophysical Journal*, 883, 192
- Bai X. N., Stone J. M., 2010, *Astrophysical Journal*, 722, 1437
- Baraffe I., Chabrier G., Allard F., Hauschildt P. H., 2002, *Astronomy and Astrophysics*, 382, 563
- Bate M. R., 2018, *Monthly Notices of the Royal Astronomical Society*, 475, 5618
- Bitsch B., Morbidelli A., Johansen A., Lega E., Lambrechts M., Crida A., 2018, *Astronomy and Astrophysics*, 612
- Borgniet S., et al., 2019, *Astronomy and Astrophysics*, 627
- Bowler B. P., et al., 2010, *Astrophysical Journal*, 709, 396
- Bressan A., Marigo P., Girardi L., Salasnich B., Dal Cero C., Rubele S., Nanni A., 2012, *Monthly Notices of the Royal Astronomical Society*, 427, 127
- Cadman J., Rice K., Hall C., Haworth T. J., Biller B., 2020, *Monthly Notices of the Royal Astronomical Society*, 492, 5041
- Chen Y.-X., Li Y.-P., Li H., Lin D. N. C., 2020, *The Astrophysical Journal*, 896, 135
- Cumming A., Paul Butler R., Marcy G. W., Vogt S. S., Wright J. T., Fischer D. A., 2008, *Publications of the Astronomical Society of the Pacific*, 120, 531
- Fischer D. A., Valenti J., 2005, *The Astrophysical Journal*, 622, 1102
- Flock M., Turner N. J., Mulders G. D., Hasegawa Y., Nelson R. P., Bitsch B., 2019, *Astronomy and Astrophysics*, 630
- Galli P. A., et al., 2021, *Astronomy and Astrophysics*, 646
- Ghezzi L., Johnson J. A., 2015, *Astrophysical Journal*, 812
- Ghezzi L., Montet B. T., Johnson J. A., 2018, *The Astrophysical Journal*, 860
- Gonzalez G., 1997, *Mon. Not. R. Astron. Soc.*, 285, 403
- Güttler C., Blum J., Zsom A., Ormel C. W., Dullemond C. P., 2010, *Astronomy and Astrophysics*, 513
- Hartmann P., 1998, *THE ASTROPHYSICAL JOURNAL*, 495, 385
- Hekker S., Meléndez J., 2007, *Astronomy and Astrophysics*, 475, 1003
- Iglesias D. P., et al., 2023, *Monthly Notices of the Royal Astronomical Society*, 519, 3958
- Ikoma M., Nakazawa K., Emori H., 2000, *The Astrophysical Journal*, 537, 1013
- Johansen A., Klahr H., 2005, *The Astrophysical Journal*, 634
- Johansen A., Oishi J. S., Low M. M. M., Klahr H., Henning T., Youdin A., 2007, *Nature*, 448, 1022
- Johansen A., Youdin A. N., Lithwick Y., 2012, *Astronomy and Astrophysics*, 537
- Johnson J. A., Aller K. M., Howard A. W., Crepp J. R., 2010, *Publications of the Astronomical Society of the Pacific*, 122
- Johnson J. A., Morton T. D., Wright J. T., 2013, *Retired a stars: The effect of stellar evolution on the mass estimates of subgiants*, doi:10.1088/0004-637X/763/1/53
- Johnston H. F., Panić O., Liu B., 2024, *Monthly Notices of the Royal Astronomical Society*, 527, 2303
- Johnston Heather F., Panić O., Liu B., Jankowski P., 2025, *Monthly Notices of the Royal Astronomical Society*, 543, 4053
- Jones M. I., Jenkins J. S., Rojo P., Melo C. H., 2011, *Astronomy and Astrophysics*, 536
- Jones M. I., Jenkins J. S., Rojo P., Olivares F., Melo C. H., 2015, *Astronomy and Astrophysics*, 580, A14
- Kanagawa K. D., Tanaka H., Szuszkiewicz E., 2018, *The Astrophysical Journal*, 861, 140
- Kennedy G. M., Kenyon S. J., 2009, *Astrophysical Journal*, 695, 1210
- Kunitomo M., Ikoma M., Sato B., Katsuta Y., Ida S., 2011, *Astrophysical Journal*, 737
- Kunitomo M., Ida S., Takeuchi T., Panić O., Miley J. M., Suzuki T. K., 2021, *The Astrophysical Journal*, 909

- Lambrechts M., Johansen A., Morbidelli A., 2014, *Astronomy and Astrophysics*, 572
- Li R., Youdin A. N., Simon J. B., 2019, *The Astrophysical Journal*, 885, 69
- Lin D. N. C., Bodenheimer P., Richardson D. C., 1996, *Nature*, 380, 606
- Liu B., Ormel C. W., 2018, *Astronomy and Astrophysics*, 615
- Liu B., Lambrechts M., Johansen A., Liu F., 2019, *Astronomy and Astrophysics*, 632, A7
- Liu B., Lambrechts M., Johansen A., Pascucci I., Henning T., 2020, *Astronomy and Astrophysics*, 638
- Liu B., Johansen A., Lambrechts M., Bizzarro M., Haugbølle T., 2022a, *Science Advances*, 8, eabm3045
- Liu B., Raymond S. N., Jacobson S. A., 2022b, *Nature*, 604, 643
- Lloyd J. P., 2011, *Astrophysical Journal Letters*, 739
- Lloyd J. P., 2013, *Astrophysical Journal Letters*, 774
- Madhusudhan N., Crouzet N., McCullough P. R., Deming D., Hedges C., 2014, *Astrophysical Journal Letters*, 791
- Manara C. F., et al., 2016, *Astronomy and Astrophysics*, 591
- Manara C. F., et al., 2017, *Astronomy & Astrophysics*, 604
- Manara C. F., Morbidelli A., Guillot T., 2018, *Astronomy and Astrophysics*, 618
- Markus Stammerl S., Lichtenberg T., Drazkowska J., Birnstiel T., 2023, *Astronomy and Astrophysics*, 670
- Mayor M., et al., 2011, *Astronomy & Astrophysics*
- Miley J. M., Panić O., Booth R. A., Ilee J. D., Ida S., Kunitomo M., 2020, *Monthly Notices of the Royal Astronomical Society*, 500, 4658
- Morbidelli A., Lambrechts M., Jacobson S., Bitsch B., 2015, *Icarus*, 258, 418
- Mortier A., Santos N. C., Sozzetti A., Mayor M., Latham D., Bonfils X., Udry S., 2012, *Astronomy and Astrophysics*, 543
- Mortier A., Santos N. C., Sousa S., Israelian G., Mayor M., Udry S., 2013, *Astronomy and Astrophysics*, 551
- Mulders G. D., Pascucci I., Apai D., 2015, *Astrophysical Journal*, 798
- Nielsen E. L., et al., 2019, *American Astronomical Society*, 158
- North T. S., et al., 2017, *Monthly Notices of the Royal Astronomical Society*, 472, 1866
- Ormel C. W., Liu B., 2018, *Astronomy and Astrophysics*, 615
- Owen J. E., Jackson A. P., 2012, *Monthly Notices of the Royal Astronomical Society*, 425, 2931
- Paardekooper S. J., Baruteau C., Kley W., 2011, *Monthly Notices of the Royal Astronomical Society*, 410, 293
- Palla F., Stahler S. W., 1993, *The Astrophysical Journal*, 418, 414
- Pan M., Liu B., Jiang L., Xie J., Zhu W., Ribas I., 2025, *The Astrophysical Journal*, 985, 7
- Pascucci I., et al., 2016, *The Astrophysical Journal*, 831, 125
- Pollack J. B., Hubickyj O., Bodenheimer P., Lissauer J. J., Podolak M., Greenzweig Y., 1996, *ICARUS*, 124, 62
- Reffert S., Quirrenbach A., Mitchell D. S., Albrecht S., Hekker S., Fischer D. A., Marcy G. W., Paul Butler R., 2006, *The Astrophysical Journal*, 652, 661
- Reffert S., Bergmann C., Quirrenbach A., Trifonov T., Künstler A., 2015, *Astronomy and Astrophysics*, 574
- Santos N. C., Israelian G., Mayor M., 2001, *Astronomy and Astrophysics*, 373, 1019
- Santos N. C., Israelian G., Mayor M., 2004, *Astronomy and Astrophysics*, 415, 1153
- Schäfer U., Yang C. C., Johansen A., 2017, *Astronomy and Astrophysics*, 597
- Schlaufman K. C., Winn J. N., 2013, *Astrophysical Journal*, 772, 143
- Shakura Sunyava 1973, *Astronomy and Astrophysics*, 24, 337
- Siess L., Dufour E., Forestini M., 2000, *ASTRONOMY AND ASTROPHYSICS*, 358, 593
- Simon J. B., Armitage P. J., Li R., Youdin A. N., 2016, *The Astrophysical Journal*, 822, 55
- Sousa S. G., Santos N. C., Israelian G., Mayor M., Udry S., 2011, *Astronomy and Astrophysics*, 533
- Stock S., Reffert S., Quirrenbach A., 2018, *Astronomy and Astrophysics*, 616
- Udry S., Santos N. C., 2007, *Annual Review of Astronomy and Astrophysics*, 45, 397
- Vioque M., Oudmaijer R. D., Baines D., Mendigutía I., Pérez-Martínez R., 2018, *Astronomy and Astrophysics*, 620
- Wagner K., Apai D., Kratter K. M., 2019, *The Astrophysical Journal*, 877, 46
- Wagner K., Apai D., Kasper M., McClure M., Robberto M., 2022, *The Astronomical Journal*, 163, 80
- Welbanks L., Madhusudhan N., Allard N. F., Hubeny I., Spiegelman F., Leininger T., 2019, *The Astrophysical Journal Letters*, 887, L20
- Wichitanakom C., Oudmaijer R. D., Fairlamb J. R., Mendigutía I., Vioque M., Ababakr K. M., 2020, *Monthly Notices of the Royal Astronomical Society*, 493, 234
- Wittenmyer R. A., Tinney C. G., Butler R. P., O’Toole S. J., Jones H. R., Carter B. D., Bailey J., Horner J., 2011, *Astrophysical Journal*, 738
- Wolthoff V., Reffert S., Quirrenbach A., Jones M. I., Wittenmyer R. A., Jenkins J. S., 2022, *Astronomy and Astrophysics*, 661
- Yang C. C., Johansen A., Carrera D., 2017, *Astronomy and Astrophysics*, 606
- Youdin A. N., Goodman J., 2005, *The Astrophysical Journal*, 620, 459
- Zhu Z., Stone J. M., Bai X.-N., 2015, *The Astrophysical Journal*, 801

This paper has been typeset from a $\text{\TeX}/\text{\LaTeX}$ file prepared by the author.